High-content assay for CFTR monitoring: simultaneous quantification of channel function and biogenesis.

Stella Prins[1], Emily Langron[1], Cato Hastings[2], Emily J. Hill[1], Andra C. Stefan[3], Lewis D. Griffin[2] and Paola Vergani[1]*

[1] Department of Neuroscience, Physiology and Pharmacology

[2] CoMPLEX

[3] Natural Sciences

University College London

Gower Street

WC1E 6BT London UK

The first two authors contributed equally to this project.

*Correspondence to: p.vergani@ucl.ac.uk

Running title: Simultaneous screening of CFTR biogenesis and function

Summary

CFTR mutations cause cystic fibrosis by affecting how many channels reach the membrane, and/or how well they work. This study presents an assay that simultaneously measures CFTR biogenesis and function. A screen of 62 disease-causing mutations provides clues on how approved drug VX-770 works.

Abstract

Cystic fibrosis (CF) is a life-limiting disease caused by mutations in the *CFTR* gene, encoding a plasma membrane anion-selective channel. Because CF-causing mutations affect both CFTR permeation/gating and biogenesis, multi-assay approaches have been implemented in drug development, sequentially screening for channel function and membrane density. Here we present the first assay capable of simultaneous assessment of both CFTR characteristics.

To validate our assay, we investigate F508del-CFTR, the most common disease-causing mutant, confirming rescue by incubation at low temperature, treatment with CFTR-targeting drugs and introduction of second-site revertant mutation R1070W. In addition, we characterize a panel of 62 CF-causing mutations and profile effects of acute treatment with approved drug VX-770 (ivacaftor). Measurements using the rare mutation panel correlate well with published results, further validating the assay. Furthermore, mapping the potentiation profile on CFTR structures raises mechanistic hypotheses on drug action, suggesting that VX-770 might allow an open-channel conformation with an alternative arrangement of domain interfaces around site 1.

The assay is a powerful tool for investigation of CFTR ion channel biophysics, allowing rapid and accurate inferences on gating/permeation properties and on how these are affected by mutations and compounds. By providing a two-dimensional molecular characterization of mutant CFTR proteins, our assay can better inform development of therapies tailored for individual CFTR variants. Finally, the integrated assay boosts the potential for discovery of dual-acting compounds, simultaneously repairing both biogenesis and function.

Keywords: protein transport, fluorescence imaging, precision medicine, VX-770.

Non-standard Abbreviations

ABC	ATP-binding cassette
CF	Cystic Fibrosis
CFTR	Cystic Fibrosis Transmembrane Conductance Regulator
$F_{\text{mCherry cell}}$	average normalized mCherry fluorescence intensity over the entire cell
$F_{\text{YFP cell}}$	average normalized YFP fluorescence intensity over the entire cell
$F_{\text{YFP membrane}}$	average normalized YFP fluorescence intensity within the membrane zone
G_{CFTR}	CFTR conductance
G_{trans}	transient anion conductance
IRES	internal ribosome entry site
NBD	nucleotide binding domain
PDL	poly-D-lysine
P_O	open probability
ρ	CFTR membrane density, as defined in this paper
SSR	sum of squared residuals
τ_{trans}	time constant of the transient anion conductance
TM	transmembrane helix
V_M	membrane potential
WT	wild type
YFP	yellow fluorescent protein

Introduction

Cystic fibrosis (CF) is a common life-limiting genetic disease. Although the median survival age has increased by almost 12 years over the last decade, the disease still strongly impacts expectation and quality of life (Elborn, 2016).

CF is caused by mutations in the *CFTR* gene (Riordan et al., 1989; Rommens et al., 1989), encoding an anion-selective channel (Csanády et al., 2019) present on the apical plasma membrane of epithelial cells. These mutations decrease the density of CFTR channels located on the cell membrane (by affecting protein synthesis, folding, intracellular trafficking, plasma membrane stability), and/or impair channel function (impacting on gating or anion permeation). As a result, transepithelial fluid movement is abnormal, creating problems particularly affecting lungs, pancreas, intestines, liver and reproductive systems.

Engineering of a halide sensitive YFP with increased affinity for iodide and a low affinity for chloride (Galietta et al., 2001a; Galietta et al., 2001b), allowed the first high throughput screening projects, which assessed CFTR activity by measuring the rate of YFP quenching caused by iodide influx and chloride efflux (Ma et al., 2002; Pedemonte et al., 2005a; Pedemonte et al., 2005b; Yang et al., 2003). Later, Vertex Pharmaceuticals used changes in membrane potential, monitored through fluorescence resonance energy transfer, to indirectly quantify CFTR channel function (Van Goor et al., 2009; Van Goor et al., 2006).

These efforts led to the identification of the first CFTR modulator drugs, directly targeting the defective CFTR protein. Modulators have been classified as either "potentiators", increasing CFTR channel function, or "correctors" increasing the number of CFTR channels on the plasma membrane. The potentiator ivacaftor (VX-770, Vertex Pharmaceuticals) (Van Goor et al., 2009) is now approved for the treatment of patients carrying the G551D gating mutation and a number of other mutations impairing channel function (Gentzsch and Mall, 2018). However, neither potentiation by VX-770 on its own (Flume et al., 2012), nor treatment with the corrector, VX-809 (Van Goor et al., 2011), alone (Clancy et al., 2012), significantly improves lung function of patients homozygous for the F508del mutation, present on at least one allele in ~90% of patients. Like many other CF-causing mutations, F508del results not only in ion channel dysfunction, but also in a reduction of the number of channels present at the cell surface. Combination treatment with VX-770 and VX-809 provides small but significant health benefits (Wainwright et al., 2015). Triple combination therapies, combining two different correctors with a potentiator, hold promise to further improve patient outcomes (Davies et al., 2018; Keating et al., 2018).

More than 300 CF-causing mutations have been characterized (The Clinical and Functional TRanslation of CFTR (CFTR2); available at http://cftr2.org). Each mutation, other than F508del, is extremely rare, and is likely to affect the folding, trafficking, stability, gating dynamics and/or permeation of the encoded CFTR protein differently. Pre-clinical data informing on how mutations and drugs affect individual CFTR variants in controlled, *in vitro* systems, is thus very valuable for drug development and trial design.

Here we present a medium-throughput image-based assay that acquires multi-dimensional data (dual-colour fluorescence intensity in time and space) on individual live HEK293 cells and extracts information on two key characteristics of CFTR. By co-expressing soluble mCherry with the halide sensitive YFP (Galietta et al., 2001a) linked to CFTR (Langron et al., 2017), our new assay gives readouts of both CFTR function, and CFTR membrane density. Experimental manipulation - incubation at low temperature (Denning et al., 1992; Rennolds et al., 2008; Wang et al., 2008), treatment with VX-809 (He et al., 2013; Okiyoneda et al., 2013) with and without VX-770 (Cholon et al., 2014; Veit et al., 2014), and addition of revertant mutation R1070W (Farinha et al., 2013; Okiyoneda et al., 2013; Thibodeau et al., 2010) - results in the expected changes in measured F508del-CFTR channel function and membrane density. Finally, we present a screening platform suitable for quantifying the molecular characteristics of 62 CFTR variants carried by CF patients, and profile the effects of VX-770 on this panel. Our results validate the assay as a valuable tool for investigation of CFTR molecular mechanism and pharmacology.

Materials and methods

Construction of the pIRES2-mCherry-YFPCFTR plasmid

The pIRES2-mCherry-YFPCFTR plasmid was obtained with two sequential subcloning steps. First, a 1.727kb region of pcDNA3.1-YFP-CFTR (Langron et al., 2017), containing the YFP-coding sequence, was subcloned into pIRES-eGFP-CFTR, a gift from David Gadsby (Rockefeller University), using the NheI and BlpI restriction sites. Subsequently a 0.737 kb region from pIRES2-mCherry-p53 deltaN (Lin et al., 2013) (Addgene), containing the mCherry-coding segment and part of the IRES, was subcloned into the pIRES-eGFP-YFPCFTR plasmid using the NotI and BmgBI/BtrI restriction sites. This resulted in the pIRES2-mCherry-YFPCFTR plasmid, with the IRES2 positioned between the two open reading frames for mCherry and YFP-CFTR.

HEK293 cell culture, transfection and incubation

HEK293 cells were maintained in Dulbecco's modified Eagle's medium (DMEM), supplemented with 2 mM L-glutamine, 100 U/ml penicillin and streptomycin, and 10% fetal bovine serum (all Life Technologies). Cells were seeded in poly-D-lysine-coated, black-walled 96-well plates (Costar, Fisher Scientific), and transiently transfected with the pIRES2-mCherry-YFPCFTR plasmid using Lipofectamine 2000 (Life Technologies). After transfection, cell plates were returned to the 37°C incubator for 24 hours. Prior to imaging plates were incubated for another 24 hours, at 37°C or 28°C, in 100 µl DMEM including DMSO (vehicle), 10 µM VX-809, or 10 µM VX-770 plus 10 µM VX-809 (Selleck Chemicals).

Image acquisition

Before imaging, cells were washed twice with 100 µL standard buffer (140 mM NaCl, 4.7 mM KCl, 1.2 mM $MgCl_2$, 5 mM HEPES, 2.5 mM $CaCl_2$,1mM glucose, pH 7.4). The ImageXpress Micro XLS (Molecular Devices), an automated inverted wide-field fluorescence microscope with a temperature-controlled chamber (set to 37°C or 28°C, as indicated), was used for image acquisition. Protocols for automated fluid additions, enabled by a robotic arm, were created using MetaXpress software (Molecular Devices). For imaging of YFP(H148Q/I152L)-CFTR, a 472 ± 30 nm excitation filter, and a 520 ± 35 nm emission filter were used. Excitation/emission filters at 531 ± 20 nm and 592 ± 20 nm were used for imaging of mCherry.

For localization of CFTR, a 60× objective was used to take 9 16-bit images per well of both fluorophores. To evaluate CFTR function, a 20× objective was used. Two 16-bit images of mCherry were taken, one at the start and one the end of the protocol. In addition, 16-bit images of the YFP fluorescence, were taken at an acquisition frequency of 0.5 Hz. For the I^- first protocol ((A), see below), after 20 s, 50 µl of 300 mM I^- buffer (300 mM NaI, 4.7 mM KCl, 1.2 mM $MgCl_2$, 5 mM HEPES, 2.5 mM $CaCl_2$,1mM glucose, pH 7.4) was added to the standard buffer, so that the final concentration of I^- in the extracellular medium was 100 mM. Another 40 s later, a further 50 µl of a 100 mM I^- buffer containing 40 µM forskolin (100 mM NaI, 4.7 mM KCl, 1.2 mM $MgCl_2$, 5 mM HEPES, 2.5 mM $CaCl_2$,1mM glucose, 40 µM forskolin, pH 7.4) was added, so that the final concentration of forskolin in the extracellular medium was 10 µM, while concentration of I^- and other components remained unaltered. For the I- last protocol ((B), below), after 20 s of imaging, CFTR was activated, in the absence of extracellular iodide, by addition of 50 µl standard buffer containing activating compounds

(forskolin or forskolin + VX-770 both to reach final concentrations of 10 μM). After a further 230 s, by which time CFTR is assumed to be gating at steady state (Langron et al., 2018), 100 mM extracellular iodide (final concentration) was introduced by adding 50 μl of iodide buffer (as standard buffer with 140 mM NaCl replaced with 400 mM NaI). Images were taken for 40 more seconds. Activating compounds were also included in the second addition so as not to alter final extracellular concentrations.

Image analysis

Image analysis was automated using MATLAB mathematical computing software (MathWorks). Separate analysis protocols were implemented to estimate CFTR membrane density and ion channel function.

CFTR membrane density

First, mCherry images were binarized, and basic morphological operations (opening, closing, area opening, and dilation) were carried out to reduce noise. A distance transform with locally imposed minima was used to segment images by means of a watershed transformation and define cell boundaries. Cells were removed from analysis if they had an area of under 108 μm^2 or over 5400 μm^2, if they had a major axis length of less than 32.4 μm, if the area over perimeter was less than 25 or over 300, and if they were touching the edge of the image. A 1.08 μm band, 10 or 5 pixels wide (depending on the resolution of the image), within the border of each cell was defined as the membrane zone.

Background was selected by inverting the binarized and morphologically opened mCherry image, after which it was morphologically closed using a large structuring element to prevent cells from being selected as background. Average background intensity was then subtracted from each pixel, and the YFP and mCherry fluorescence intensity of each cell was normalized to the median YFP and mCherry fluorescence intensities of cells expressing WT-CFTR on the same plate. If the average normalized fluorescence intensity fell below 0 (due to low transfection efficiency and high background noise), cells were removed from analysis.

In order to estimate CFTR membrane density for each cell (defined as ρ, see Results), the average normalized YFP fluorescence intensity within the membrane zone was divided by the average normalized mCherry fluorescence over the entire cell.

$$\rho = \frac{F_{\text{YFP membrane}}}{F_{\text{mCherry cell}}}$$

CFTR ion channel function

For assessment of CFTR function, two different protocols were used. For both, cells were selected based on the mCherry fluorescence image that was taken at the beginning of the protocol.

(A) I^- first Protocol

The fluorescence at the time point before addition of I^- was used to normalize YFP fluorescence intensity. The concentration of I^- inside the cells ($[I^-]_{in}$) can be estimated with the following equation (Langron et al., 2017), in which the binding affinity for I^- (K_I) to YFP(H148Q/I152L) is 1.9 mM (Galietta et al., 2001a) and the normalized fluorescence intensity over time ($F(t)$) is determined experimentally.

$$[I^-]_{in} = K_I \frac{(1 - F(t))}{F(t)}$$

Data is collected every 2 seconds, so the change $[I^-]_{in}$ observed at each time point can be estimated and used to calculate the rate of I^- entry (in mM/s):

$$\frac{\Delta[I^-]_{in}}{\Delta t} = \frac{[I^-]_{in}(t) - [I^-]_{in}(t-1)}{2\ \mathrm{s}}$$

The maximal observed rate of I^- entry is used as a measure of cellular anion conductance. To determine whether there was increased CFTR-mediated anion conductance, the maximal rate of I^- entry after addition of forskolin (which activates CFTR by cAMP dependent phosphorylation), was compared to the maximal rate of I^- entry after addition of DMSO (vehicle, negative control).

(B) I^- last Protocol

CFTR activation (by addition of 10 μM forskolin with or without 10 μM VX-770, as indicated) was first allowed to reach steady state in the absence of I^- and quenching of YFP in the 40 s following extracellular I^- addition was measured. A simple mathematical model was used to fit observed fluorescence quenching, and estimate CFTR conductance as described (Langron et al., 2018). Briefly, the model includes four free parameters: CFTR conductance at steady-state (G_{CFTR}), membrane potential at steady-state, immediately prior to I^- addition (V_M), and conductance (G_{trans}) and time constant (τ_{trans}) of a transient, endogenous non-CFTR anion conductance. The values of the four parameters were estimated by minimizing the sum of squared residuals obtained by comparing the time course of the observed average fluorescence intensity within cells to the proportion of anion-free YFP chromophore predicted by the model (both normalized to the time point before I^- addition). However, when the quenching time course was too fast and did not provide enough information to uniquely identify all four

parameters, the value of the latter two parameters (G_{trans} and τ_{trans}) was constrained to the average values obtained with negative controls, and only G_{CFTR} and V_M were estimated (Langron et al., 2018).

For both protocol (A) and (B) the value obtained from analysis of the observed YFP-CFTR fluorescence quenching ($\frac{\Delta[I^-]_{in}}{\Delta t}$ and G_{CFTR}, respectively) was corrected to account for variations in transfection efficiency. Thus the metric reporting ion channel function was normalised for each condition/genotype by dividing by the mean $F_{mCherry}$ within the cell selection (which, in turn, was normalized to $F_{mCherry}$ measured for WT in the same plate).

Data and Statistical analysis

Measurements of conductance from the rare mutation panel were obtained on 3 or 4 independent plates (each plate containing at least 3 wells per mutant, per condition). As demonstrated by the good correlation with published datasets (see Results and Supplementary Figure S8) this is sufficient to give a first characterization of ion channel function, as is required for most screens. Because ρ values approach a log-normal distribution, values were log transformed before performing statistical analysis, allowing parametric testing of the data.

To determine whether the observed differences in ρ, $\frac{\Delta[I^-]_{in}}{\Delta t}$, or G_{CFTR} resulting from experimental manipulation and/or mutations were statistically significant, we performed either independent or paired t-tests. For ρ measurements, we noticed that some variability could be accounted for by variation among plates, and paired comparisons between treatments/genotypes measured from the same plate increased our power to detect small differences. When required, either a Bonferroni or a Benjamini-Hochberg correction was applied to adjust for multiple comparisons. Data in graphs represent mean ± SEM, and the significance level was pre-specified as $\alpha = 0.05$. Statistical analysis was carried out using MATLAB (MathWorks), SigmaPlot (Systat Software), SPSS (IBM), or Excel (Microsoft).

Supplemental Material

Tables are given with more information on the statistical analyses performed (S1-S4, S6, S7). Figure S5 compares distributions of $\log_{10}\rho$ values of WT-CFTR with each mutant in the rare mutation panel, as well as plots illustrating the paired t-tests performed. Figure S8 compares the rare mutation results presented here with two published datasets (Sosnay et al., 2013; Van Goor et al., 2014). Figure S9 and Table S10 give further information regarding the analysis used to obtain Figures 4B and 5A.

Results

The assay

To obtain quantitative information about ion channel function of CFTR, we exploited a halide-sensitive YFP (Galietta et al., 2001a; Galietta et al., 2001b), tagged to the N-terminal of CFTR (Langron et al., 2018; Langron et al., 2017). We constructed a pIRES2-mCherry-YFPCFTR plasmid that directs co-expression of YFP(H148Q/I152L)-CFTR (hereafter designated YFP-WT-CFTR or simply WT-CFTR) and a soluble, cytosolic, red fluorescent protein, mCherry (Shaner et al., 2004) (Figure 1A). The mCherry expression allows image segmentation and localization of the cell membrane by marking the border of cells. Furthermore, mCherry serves as an internal standard for the normalisation of YFP-CFTR expression, eliminating variability due to unequal transfection efficiency.

Yellow fluorescence at the boundaries of areas of red fluorescence is used to estimate CFTR membrane density for each cell (Figure 1). The "membrane" is defined as comprising a ~1 μm wide band, on the inside of a cell's boundary. The density of CFTR at the membrane (ρ), is estimated by dividing the average YFP-CFTR fluorescence intensity within the membrane zone ($F_{\text{YFP membrane}}$), by the average mCherry fluorescence over the entire cell ($F_{\text{mCherry cell}}$). The ρ metric can be thought of as the product of the proportion of CFTR localized to the membrane ($F_{\text{YFP membrane}}/F_{\text{YFP cell}}$), multiplied by the metabolic stability of YFP-CFTR with respect to mCherry ($F_{\text{YFP cell}}/F_{\text{mCherry cell}}$). Thus, changes in ρ metric will reflect not only changes in CFTR trafficking, but also changes in the overall rates of biosynthesis vs. degradation of the protein.

Increasing F508del-CFTR membrane density

To validate our assay, we assessed changes in F508del-CFTR membrane density by comparing distributions of $\log_{10}\rho$ (logarithmic transformation of the ρ metric) obtained from thousands of cells for each genotype/condition (Figure 2).

<u>F508del-CFTR: VX-809 incubation</u>

At 37°C, incubation with VX-809 for 24 hours caused a small but significant increase in $\log_{10}\rho$ of F508del-CFTR, (Figure 2A left, see also Supplementary Table S1). At 28°C, the magnitude of the increase was greater (Figure 2A right).

<u>F508del-CFTR: R1070W second-site revertant mutation</u>

Introducing the second-site revertant mutation R1070W (Thibodeau et al., 2010) in the F508del-CFTR background, significantly increased membrane density at 37°C, (Figure 2B left, Supplementary Table S1), as well as at 28°C (Figure 2B right, Supplementary Table S1). Again, the magnitude of the effect was larger at 28°C.

F508del-CFTR: chronic VX-770 incubation

When comparing cells expressing F508del-CFTR incubated for 24 hours with VX-809 alone, with those incubated with both VX-809 and VX-770, at 37°C, there was a small but significant decrease in $\log_{10}\rho$ (Figure 2C left, Supplementary Table S1). At 28°C the decrease was again more pronounced than at 37°C (Figure 2C right).

F508del-CFTR: temperature correction

Because our fluorescence readings are normalized to those obtained from cells expressing WT-CFTR grown on the same 96-well plate, we quantified the difference between the mean $\log_{10}\rho$ of WT-CFTR and F508del-CFTR at each temperature. The $\log_{10}\rho$ values of F508del-CFTR were found to be significantly closer to those of WT-CFTR at 28°C, than at 37°C, (Figure 2D, Supplementary Table S1).

Increasing F508del-CFTR ion channel function

Following addition of extracellular I^- (I^- first Protocol, see Methods), CFTR was activated by 10 μM forskolin alone, or by a combination of 10 μM forskolin and 10 μM VX-770 (the latter defined as an acute (a) treatment, as opposed to the 24-hour chronic (c) incubation with VX-770 described above). The normalized fluorescence of HEK293-cells expressing YFP-tagged WT-CFTR, F508del-CFTR, or F508del/R1070W-CFTRwas followed over time (Figure 3). The maximal rate of I^- entry was used to summarize CFTR channel function for the different CFTR genotypes, incubation and activation conditions tested (Figure 3E, Supplementary Tables S2 and S3). No significant difference in this metric was detected among the different genotypes/conditions when DMSO (vehicle) was added instead of activators.

WT-CFTR

As expected, in cells expressing WT-CFTR, the maximal rate of I^- entry was significantly higher after activation with forskolin, compared to control (DMSO), at both 37°C and 28°C

(Figure 3A; Figure 3E WT). However, neither the presence of 10 μM VX-770 in addition to forskolin during activation, nor incubation at 37°C vs. 28°C modified quenching rate sufficiently to achieve statistical significance after multiple comparison correction (Figure 3A; Figure 3E, WT, Supplementary Table S3).

F508del-CFTR: activation following temperature correction

Activation with forskolin alone failed to increase the maximal rate of I^- entry in untreated cells expressing F508del-CFTR (Figure 3B top; Figure 3E F508del bars 1 and 4, Supplementary Table S2), reflecting the severe gating defect which persists even after temperature correction. Acute potentiation by VX-770 was required to detect function of the channels reaching the cell surface thanks to temperature-correction (Figure 3B, bottom; Figure 3E F508del bars 5 vs. 2, Supplementary Table S2).

F508del-CFTR: activation following VX-809 correction

At both temperatures, the activity of F508del-CFTR channels reaching the cell surface after 24-hour incubation with VX-809 could be detected following acute activation with forskolin and VX-770. At 28°C the maximal rate of I^- entry was significantly greater than at 37°C (Figure 3C; Figure 3E, F508del bar 6 vs. 3, Supplementary Table S3).

F508del-CFTR: rescue of ion channel function by the R1070W mutation

Forskolin activation alone was enough to reveal F508del/R1070W-CFTR channel activity (Figure 3D, Supplementary Table S2). The maximal rate of I^- entry was significantly higher at 28°C than at 37°C (Figure 3D; Figure 3E F508del/R1070W, Supplementary Table S3).

The rare mutation panel

CF-causing missense CFTR mutations (Sosnay et al., 2013; Van Goor et al., 2014; Yu et al., 2012) were individually introduced in the pIRES2-mCherry-YFPCFTR plasmid, creating a panel of 62 plasmids (including WT-CFTR as reference).

Following expression of the panel in HEK293 cells, and incubation with no pharmacological correction, distributions for the ρ metric, and plate $\log_{10}\rho$ means were obtained (Supplementary Table S4, Supplementary Figure S5). The data is summarized in Figure 4A, which profiles membrane density for each CFTR mutant in the panel. Correlation between our measured ρ and the proportion of CFTR acquiring complex glycosylation in FRT

cells is surprisingly good (r^2 = 0.65, Sosnay et al., 2013; r^2 = 0.48, Van Goor et al., 2014, Supplementary Figure S8), considering the differences in expression system and metric used (note that correlation between the two published datasets is r^2 = 0.48).

YFP-CFTR fluorescence quenching experiments (I^- last Protocol, see Methods) were carried out to estimate steady-state CFTR conductance (G_{CFTR}), without (DMSO) and with baseline CFTR activation by 10 µM forskolin (Figure 4B-C; Supplementary Table S6). Again, results correlate well with published data (r^2 = 0.68, Sosnay et al., 2013; r^2 = 0.60 Van Goor et al., 2014; Supplementary Figure S8). Conductance was also measured in the presence of 10 µM forskolin + 10 µM VX-770 (Figure 4B, D; Supplementary Table S7). In these conditions, genotypes with high conductance (including WT-CFTR) have faster YFP quenching than can be reliably measured in our system. However, the assay can accurately monitor VX-770 potentiation when CFTR activity is low, as is the case for most mutants (Van Goor et al., 2014).

Relationship between CFTR ion channel function and membrane density

By considering the changes in ion channel function in the context of any changes measured in ρ, our assay allows more accurate inferences on the gating and permeation properties of the CFTR channel molecules present at the cell surface.

Even when virtually no channels are present in the plasma membrane (as happens, for instance, for cells expressing F508del-CFTR incubated at 37^0 C) the value of ρ does not fall to zero. This is likely due to some inaccuracy in automated cell boundary detection and to the widefield microscope optics, resulting in stray light from out-of-focus planes reaching the photomultiplier. To empirically investigate the relationship between G_{CFTR} and ρ, cells expressing F508del-CFTR were treated with increasing concentrations of corrector VX-809, progressively improving both biogenesis/membrane stability and conductance (Figure 5A; Supplementary Figure S9). Measured G_{CFTR} values as a function of ρ values show a roughly linear relationship. The trendline can be extended to cross the ρ axis, extrapolating to an intercept at ρ = 0.23. In addition, extension towards higher membrane densities shows how gating of F508del-CFTR, VX-809-corrected and acutely potentiated by VX-770, reaches levels characteristic of WT-CFTR (without potentiation), consistent with patch-clamp open probability (P_O) measurements (Kopeikin et al., 2014; Wang et al., 2018).

Data on maximum rate of I^- entry can also be plotted against the corresponding ρ values, measured for the different F508del-CFTR rescue strategies (Figure 5B). A linear interpolation between data points for uncorrected F508del-CFTR at 37^0 C (representing cells with virtually no CFTR molecules at the membrane) and WT-CFTR activated by 10 μM forskolin at 37^0 C describes the ion channel function we would expect from cells with increasing CFTR membrane density, assuming gating and permeation characteristics of baseline-activated WT-CFTR. This allows us to infer how rescued F508del-CFTR channels reaching the membrane compare to control channels in terms of function.

Introducing the R1070W revertant mutation in the F508del-CFTR background is shown to be particularly effective in improving gating. Comparing revertant rescue with temperature correction, Figure 5B shows how both strategies similarly increase membrane density but temperature-corrected F508del-CFTR channels at the membrane have very low ion channel function (unless acutely potentiated with VX-770). In contrast, F508del/R1070W channels at the membrane have gating and permeation properties equal - or even superior - to WT-CFTR (Figure 5B, cf. F508del/R1070W-CFTR red symbol vs. uncorrected F508del-CFTR blue symbol). Both results are consistent with patch-clamp records indicating a F508del/R1070W-CFTR P_O comparable to that of WT-CFTR (Liu et al., 2018), but a much lower P_O for temperature-corrected F508del-CFTR (Kopeikin et al., 2014; Liu et al., 2018; Wang et al., 2018) – note that single-channel conductance, γ, is unaffected by F508del and R1070W mutations (Dalemans et al., 1991; Thibodeau et al., 2010).

Plots of G_{CFTR} as a function of ρ for the rare-mutation panel give an overview of processing and gating/permeation defects caused by each missense mutation (Figure 5C). For instance, D579G-CFTR (orange open diamond at coordinates (0.35,41.5)) falls close to the WT-CFTR interpolation line, suggesting that the product of channel P_O and γ is not greatly affected by this mutation, and that the low short-circuit currents measured in FRT cells (Sosnay et al., 2013; Van Goor et al., 2014) are largely caused by the reduced membrane density. For G1244E (orange (0.75,7.2)) and S549N (blue (0.83,11)), likely altering the structure of P- and signature sequence loops, respectively, in site 2, measured ion channel function is much lower than would be expected given the high membrane density. Here low short-circuit currents (Sosnay et al., 2013) are likely due to gating defects. Most mutations give reduced membrane densities and a conductance that falls below the interpolation line, suggesting processing defects as well as some degree of impairment in gating/permeation for the molecules that do

reach the membrane. We further illustrate the effect of acute treatment with VX-770 for mutations resulting in the strongest potentiation (fold-potentiation >20, Figure 5D). For many of these, data points for potentiated conductance fall above the interpolation line, suggesting that $P_O \cdot \gamma$ is higher than measured for WT-CFTR in baseline-activated conditions.

Discussion

Validation of the assay and implications for pharmacological research

Many CFTR variants associated with CF, including the most common, F508del-CFTR, are characterized by both processing and functional defects. Rescue of either ion channel function or membrane density alone, is not enough for effective treatment of patients carrying F508del-CFTR (Clancy et al., 2012; Flume et al., 2012), or many other mutations. Therapies combining multiple correctors/potentiators are now seen as most promising (Holguin, 2018). However, potentiators can negatively interfere with corrector action (Cholon et al., 2014; Meng et al., 2017; Veit et al., 2014). Furthermore, it has been suggested that maintaining a clear separation between correctors and potentiators does not usefully describe CFTR pharmacology (Rowe and Verkman, 2013). Practical implementation of distinct potentiator and corrector screens might have biased the search towards combination therapies, hampering discovery of modulators with true dual activity. All this highlights the potential impact of our assay, capable of simultaneously measuring pharmacological effects on membrane localization and on gating/permeation characteristics.

Membrane density

Our assay accurately detects changes in membrane density of CFTR, even when such changes are small and the heterogeneity among cells is large. It can pick up the minute difference in membrane density between untreated and VX-809 treated HEK293 cells incubated at 37°C (Figure 2A left). The VX-809 effect is undetectable, unless combined with temperature rescue or revertant mutations, in other systems (e.g. Okiyoneda et al., 2013). The effect of the R1070W mutation on F508del-CFTR membrane density at 37°C is similarly small (Okiyoneda et al., 2013) but our assay detects a significant difference (Figure 2B left). We were also able to confirm that the membrane density of F508del-CFTR is increased at low temperature (Denning et al., 1992; Rennolds et al., 2008; Wang et al., 2008, Figure 2D). The effects of VX-809 treatment (He et al., 2013) and R1070W rescue on membrane density are larger when combined with incubation at low temperature (Figure 2 right). In agreement with

other studies (Cholon et al., 2014; Meng et al., 2017; Veit et al., 2014), we observed a small but significant shift in $\log_{10}\rho$ following chronic incubation with VX-770, consistent with the potentiator destabilizing F508del-CFTR at the membrane (Figure 2C left). Furthermore, we find that the negative effect of VX-770 on biogenesis appears more pronounced when cells are incubated at 28°C (Figure 2C). It is possible that binding of VX-770 prevents interaction with chaperone(s) which help F508del-CFTR fold and exit the ER in HEK293 cells grown at low temperature (Wang et al., 2008). However, further studies are required to confirm our observation and its physiological relevance. First, at 37°C the small signal from membrane-localised F508del-CFTR might prevent us from accurately quantifying the effect of adding VX-770 to the incubation. Second, given the high [VX-770] used (Csanády and Töröcsik, 2019; Matthes et al., 2016), some of the F508del-CFTR destabilization we observe might be linked to formation of precipitates within cellular membranes, which might be more pronounced at the lower temperature. We note, however, that in our HEK293 incubation medium, as in plasma, a large proportion of the drug will be bound to proteins present in the added serum (Matthes et al., 2016).

Ion channel function

In addition to membrane density, our assay quantifies channel function. Here, the assay is not optimized to measure high CFTR activities and some measurements hit the upper limit of its dynamic range (e.g. for WT-CFTR, Figs. 3 and 4, Supplementary Table S3). However, both the "I^- first" protocol (Langron et al., 2017), measuring the maximal rate of I^- entry ($\frac{\Delta[I^-]_{in}}{\Delta t}$) during CFTR activation, and "I^- last" protocol (Langron et al., 2018), estimating CFTR conductance by fitting quenching time course after steady-state activation is reached, can accurately quantify the low CFTR activities typically seen in mutants. While the "I^- last" protocol is unaffected by variability in signal transduction kinetics and better accounts for changing electrochemical potential gradients, the "I^- first" protocol allows faster data acquisition and less computationally intensive analysis. In line with results obtained with other techniques (e.g. Ussing chambers, high-throughput electrophysiology), our results show that both G_{CFTR} (Sosnay et al., 2013; Van Goor et al., 2014, Supplementary Figure S8) and $\frac{\Delta[I^-]_{in}}{\Delta t}$ (Billet et al., 2017; Van Goor et al., 2011, Figures 3, 5B) provide accurate estimates of CFTR activity.

Accurate quantification of low conductance values is advantageous in characterizing drug response by CFTR mutants, most of which have low residual activity. Our assay detects strong VX-770 potentiation for R347P-, N1303K- and H1085R-CFTR, genotypes giving no

significant potentiation over baseline in the Ussing chamber study (Van Goor et al., 2014). Equally, L927P- and H1045D-CFTR channels are seen to be powerfully potentiated in our assay. Acute treatment with VX-770 is most effective on L927P channels, resulting in an ~80-fold potentiation. L927P is adjacent to A928, part of the VX-770 binding site (Liu et al., 2019). Our results on N1303K are consistent with patch-clamp results demonstrating effective potentiation by VX-770 (DeStefano et al., 2018). Despite Cl^- permeability in FRT cells being increased only to less than 5% of WT-CFTR-expressing cells (Van Goor et al., 2014), caution is required in classifying all such mutants as "unresponsive" to VX-770. Further investigation of possible synergies/drug-drug interactions will be required as it is likely that they might benefit from therapies combining VX-770 with other modulators, as has been proposed (DeStefano et al., 2018; Phuan et al., 2018): patch-clamp recording of how the ion channel function of these mutants is altered by simultaneous binding of VX-770 and other modulators, and studies on chronic rather than acute treatment.

While other functional assays, in more native systems (e.g. Ussing chamber measurements on human bronchial epithelia), will remain the "gold standard" for testing of CFTR-targeting drugs, providing licensing authorities with material on which to base decisions on treatment of patients with genotypes found only extremely rarely in the population (Ratner, 2017), our assay could usefully complement these and other techniques, especially if throughput is further increased (the assay is currently run using 96-well plates but small changes could make it compatible to a 384 well plate format). Describing each CF-causing mutation with two coordinates (ρ and G_{CFTR}) is a concise, informative way of characterizing mutations (e.g. Figure 5C) and the effects of CFTR modulators on them (e.g. Figure 5D). Implementing the assay at early stages (compound screening and structure-activity relationship studies) could better inform development of genotype-tailored therapies and give valuable insight relevant to patient stratification for clinical trial planning. In addition, our high-content assay boosts the potential for discovery of drugs simultaneously repairing both defects (correcting CFTR biogenesis and potentiating its function), and its exploitation might result in successful identification of effective and potent dual-activity modulators, a feat that has so far eluded extensive compound screens (but note proof-of-principle demonstration in Phuan et al., 2015; Phuan et al., 2011).

Considerations on VX-770 binding and mechanism of action

Empirical profiling of drug effects on the rare mutation panel can generate hypotheses on mechanism of action. Considering the sites of mutations resulting in the highest VX-770 efficacy (fold-potentiation >20, Figure 5D), these appear to link the ATP molecule bound at site 1 (comprising Walker motifs of NBD1 and signature sequence of NBD2) to regions close to the narrowest portion of the permeation pathway, thought to constitute the CFTR gate (El Hiani and Linsdell, 2010; Gao and Hwang, 2015), and positioned adjacent to the very recently identified VX-770 binding site (Liu et al., 2019) (Figure 6).

Among the highly VX-770-sensitive mutations, all those surrounding the ATP and NBD/TMD interface introduce charged side chains which would interact unfavourably with other close charges in the conformation observed for phosphorylated, ATP-bound human CFTR, carrying the open-state stabilizing E1371Q mutation, 6MSM (Zhang et al., 2018b): the aspartate replacing G1349, in the NBD2 signature sequence, with the γ-phosphate bound at site 1 (Bompadre et al., 2007); the lysine in place of N1303 in the NBD2 "socket", with R1358 in NBD2; the arginine replacing G178, in intracellular loop 1 (ICL1) with K254, E257 and R258 in ICL2 (Zhang et al., 2018b); the aspartate replacing H1054, in ICL4, with E543 in the NBD1 X-loop (He et al., 2008); the arginine in place of H1085, with R1048 in transmembrane helix 10, TM10 (for all listed pairs distances between α-carbons in 6MSM are below 10 Å). Mutations at these sites are likely to particularly destabilize the NBD-dimerized, ABC-canonical open channel conformation, making occupancy of these states a rare event. Consistent with this interpretation, N1303K-CFTR channels appear to have almost completely lost the coupling between NBDs and TMDs that normally controls gating, and the rare openings observed are not linked to ATPase cycles at the NBDs (DeStefano et al., 2018). The fact that for all these mutants conductance is greatly increased by VX-770 suggests that drug binding might allow these channels to reach an alternative, particularly stable, open state, with a different conformation at the interface between site 1 and the TMDs.

It has been recently suggested that "undocking" of NBD1 from the TMDs might occur physiologically (Sigoillot et al., 2019) and a recent finding hints at the possibility that the VX-770-bound open state might comprise an undocked NBD1. The coupling helix in ICL4, buried at the interface between TMDs and NBD1 in all the CFTR structures so far reported, was identified as the region for which VX-770 binding decreases hydrogen/deuterium exchange most (Byrnes et al., 2018), as would be expected if this helix forms part of a drug-binding site. While the recent cryo-EM structure of the E1371Q CFTR mutant in complex with VX-770 shows density for only one VX-770 molecule, bound in the transmembrane region (Liu et al.,

2019), it is possible that the exceptionally stable NBD1/NBD2 dimer of this mutant prevents VX-770 access to a second binding site at the ICL4/NBD1 interface. In contrast, in WT and other mutants, NBD1 undocking might expose this second site. It is interesting to note that binding of a drug at a site between TM4, TM5 and TM6 (not far from the transmembrane VX-770 binding site on CFTR) in the MsbA bacterial ABC exporter, leads to a conformational change in TM4 which is transmitted to the NBDs and results in the unusual displacement of one NBD, undocking it from the conserved network of molecular interactions generally observed at the NBD/TMD interface (Ho et al., 2018). NBD undocking in VX-770-bound CFTR, by altering the NBD1/NBD2 interface might result in deocclusion of one of the interfacial ATP-binding sites. Occupancy of this low affinity ATP-binding site, accessible on open channels, might underlie the observed prolongation of open dwell-time with increasing [ATP] (Jih and Hwang, 2013). A second VX-770 binding site, exposed by infrequent undocking of NBD1 would also be consistent with the very slow activation time-course observed upon addition of VX-770 to WT-CFTR, likely reflecting VX-770 having to sequentially occupy two sites before the P_O can increase (Csanády and Töröcsik, 2019).

The remaining two highly VX-770-sensitive mutations we identify, R347P and L927P (Figures 5D,6) insert prolines, known to restrict backbone flexibility, in a region close to the CFTR gate. R347, in TM6, is important for maintaining a stable conducting pathway (Cotten and Welsh, 1999; Cui et al., 2013; Kopeikin et al., 2010), while L927 is in the unwound segment of TM8 (Corradi et al., 2018; Liu et al., 2017), underlying CFTR's unique channel function (Liu et al., 2017). The very low conductance measured after baseline activation in both these mutants, suggests that backbone flexibility at both these sites is required for channel opening and/or to maintain an open permeation pathway (Zhang et al., 2018b). VX-770 has been hypothesized to increase conformational flexibility of CFTR (Cholon et al., 2014) overall. It is possible that this increased flexibility might particularly concern regions surrounding bound VX-770 facilitating rearrangement of the helices, allowing adoption of the alternative open state described above.

Conclusions

The main advantage of our assay consists in providing simultaneous measurements of ion channel function and membrane density. Currently available high throughput assays report on either CFTR surface expression or CFTR-mediated cellular conductance (G_{CFTR}). G_{CFTR} is the product of 3 factors: the number of channels at the membrane (N), P_O, and γ (i.e. $G_{CFTR} = N \cdot P_O \cdot \gamma$). Being able to monitor how compounds or mutations affect both number of channels

at the membrane and conductance can allow accurate deconvolution of effects on processing (altering *N*) from those influencing gating and permeation of the channel (affecting P_O and γ, respectively). Thus, used in combination with other techniques (e.g. patch-clamp, molecular dynamics and Ussing chamber measurements), the assay is a powerful tool for basic research on CFTR biophysics and biogenesis, as well as for translational research on CFTR-targeting drugs.

Finally, because CFTR plays an important role controlling fluid transport across several epithelia (Frizzell and Hanrahan, 2012; Saint-Criq and Gray, 2017), it has been implicated in a number of pathologies, including COPD (Solomon et al., 2017; Zhao et al., 2014), secretory diarrhoeas (Thiagarajah et al., 2015), polycystic kidney disease (Li et al., 2012) and others (Solymosi et al., 2013; Zhang et al., 2018a). It is likely that, given the complexity of CFTR folding and trafficking (Farinha and Canato, 2017; Lukacs and Verkman, 2012), many CFTR-targeting compounds will alter its cellular processing (Clunes et al., 2012), suggesting that the assay could also be usefully deployed in the development of novel CFTR-targeting drugs for other diseases, beyond CF.

Author Contributions

Experiments were conceived and designed by SP, EL and PV, after discussion with LDG and CH. SP and EL, with the help of ACS, CH and EJH, carried out the molecular biology, ran the fluorescence assay acquisition and ran image analysis. SP, with the help of CH, implemented the image analysis protocols and the mathematical model in the MATLAB environment. Manuscript was written by SP, EL and PV. All authors read and commented on the final draft of the manuscript.

Acknowledgements

EL was supported by grant 15UCL04, funded by the Sparks charity and Cystic Fibrosis Trust. SP was supported by grant SRC005 funded by the Cystic Fibrosis Trust. CH was supported by EPSRC grant EP/F500351/1, and ACS was awarded a British Pharmacological Society Vacation Studentship. We thank Dr William Andrews, Central Molecular Laboratory, UCL for help with molecular biology.

Conflict of interest declaration

The authors declare no conflicts of interest.

620 **References**

621 Billet A, Froux L, Hanrahan JW, and Becq F (2017). Development of Automated Patch
622 Clamp Technique to Investigate CFTR Chloride Channel Function. Front Pharmacol 8.
623
624 Bompadre SG, Sohma Y, Li M, and Hwang T-C (2007). G551D and G1349D, Two CF-
625 associated Mutations in the Signature Sequences of CFTR, Exhibit Distinct Gating Defects. J
626 Gen Physiol 129: 285-298.
627
628 Byrnes LJ, Xu Y, Qiu X, Hall JD, and West GM (2018). Sites associated with Kalydeco
629 binding on human Cystic Fibrosis Transmembrane Conductance Regulator revealed by
630 Hydrogen/Deuterium Exchange. Scientific Reports 8: 4664.
631
632 Cholon DM, Quinney NL, Fulcher ML, Esther CR, Das J, Dokholyan NV, et al. (2014).
633 Potentiator ivacaftor abrogates pharmacological correction of deltaF508 CFTR in cystic
634 fibrosis. Sci Transl Med 6: 246ra296.
635
636 Clancy JP, Rowe SM, Accurso FJ, Aitken ML, Amin RS, Ashlock MA, et al. (2012). Results
637 of a phase IIa study of VX-809, an investigational CFTR corrector compound, in subjects
638 with cystic fibrosis homozygous for the F508del-CFTR mutation. Thorax 67: 12-18.
639
640 Clunes LA, Davies CM, Coakley RD, Aleksandrov AA, Henderson AG, Zeman KL, et al.
641 (2012). Cigarette smoke exposure induces CFTR internalization and insolubility, leading to
642 airway surface liquid dehydration. FASEB J 26: 533-545.
643
644 Corradi V, Gu R-X, Vergani P, and Tieleman DP (2018). Structure of Transmembrane Helix
645 8 and Possible Membrane Defects in CFTR. Biophys J 114: 1751-1754.
646
647 Cotten JF, and Welsh MJ (1999). Cystic Fibrosis-associated Mutations at Arginine 347 Alter
648 the Pore Architecture of CFTR. Evidence for disruption of a salt bridge. J Biol Chem 274:
649 5429-5435.
650
651 Csanády L, and Töröcsik B (2019). Cystic fibrosis drug ivacaftor stimulates CFTR channels
652 at picomolar concentrations. eLife 8: e46450.

Csanády L, Vergani P, and Gadsby DC (2019). STRUCTURE, GATING, AND REGULATION OF THE CFTR ANION CHANNEL. Physiol Rev 99: 707-738.

Cui G, Freeman CS, Knotts T, Prince CZ, Kuang C, and McCarty NA (2013). Two Salt Bridges Differentially Contribute to the Maintenance of Cystic Fibrosis Transmembrane Conductance Regulator (CFTR) Channel Function. J Biol Chem 288: 20758-20767.

Dalemans W, Barbry P, Champigny G, Jallat S, Jallat S, Dott K, et al. (1991). Altered chloride ion channel kinetics associated with the [Delta]F508 cystic fibrosis mutation. Nature 354: 526-528.

Davies JC, Moskowitz SM, Brown C, Horsley A, Mall MA, McKone EF, et al. (2018). VX-659–Tezacaftor–Ivacaftor in Patients with Cystic Fibrosis and One or Two Phe508del Alleles. N Engl J Med 379: 1599-1611.

Denning GM, Anderson MP, Amara JF, Marshall J, Smith AE, and Welsh MJ (1992). Processing of mutant cystic fibrosis transmembrane conductance regulator is temperature-sensitive. Nature 358: 761-764.

DeStefano S, Gees M, and Hwang T-C (2018). Physiological and pharmacological characterization of the N1303K mutant CFTR. Journal of Cystic Fibrosis.

El Hiani Y, and Linsdell P (2010). Changes in Accessibility of Cytoplasmic Substances to the Pore Associated with Activation of the Cystic Fibrosis Transmembrane Conductance Regulator Chloride Channel. J Biol Chem 285: 32126-32140.

Elborn JS (2016). Cystic fibrosis. The Lancet 388: 2519-2531.

Farinha CM, and Canato S (2017). From the endoplasmic reticulum to the plasma membrane: mechanisms of CFTR folding and trafficking. cell Mol Life Sci 74: 39-55.

Farinha CM, King-Underwood J, Sousa M, Correia Ana R, Henriques Barbara J, Roxo-Rosa M, et al. (2013). Revertants, Low Temperature, and Correctors Reveal the Mechanism of

687 F508del-CFTR Rescue by VX-809 and Suggest Multiple Agents for Full Correction. Chem
688 Biol 20: 943-955.
689
690 Flume PA, Liou TG, Borowitz DS, Li H, Yen K, Ordoñez CL, et al. (2012). Ivacaftor in
691 subjects with cystic fibrosis who are homozygous for the f508del-cftr mutation. Chest 142:
692 718-724.
693
694 Frizzell RA, and Hanrahan JW (2012). Physiology of Epithelial Chloride and Fluid Secretion.
695 Cold Spring Harb Perspect Med 2.
696
697 Galietta L, Haggie P, and Verkman A (2001a). Green fluorescent protein-based halide
698 indicators with improved chloride and iodide affinities. FEBS Lett 499: 220-224.
699
700 Galietta L, Jayaraman S, and Verkman A (2001b). Cell-based assay for high-throughput
701 quantitative screening of CFTR chloride transport agonists. Am J Physiol Cell Physiol 281:
702 C1734-C1742.
703
704 Gao X, and Hwang T-C (2015). Localizing a gate in CFTR. Proceedings of the National
705 Academy of Sciences of the United States of America 112: 2461-2466.
706
707 Gentzsch M, and Mall MA (2018). Ion Channel Modulators in Cystic Fibrosis. Chest 154:
708 383-393.
709
710 He L, Aleksandrov AA, Serohijos AWR, Hegedus T, Aleksandrov LA, Cui L, et al. (2008).
711 Multiple Membrane-Cytoplasmic Domain Contacts in the Cystic Fibrosis Transmembrane
712 Conductance Regulator (CFTR) Mediate Regulation of Channel Gating. J Biol Chem 283:
713 26383-26390.
714
715 He L, Kota P, Aleksandrov AA, Cui L, Jensen T, Dokholyan NV, et al. (2013). Correctors of
716 deltaF508 CFTR restore global conformational maturation without thermally stabilizing the
717 mutant protein. FASEB J 27: 536-545.
718
719 Ho H, Miu A, Alexander MK, Garcia NK, Oh A, Zilberleyb I, et al. (2018). Structural basis
720 for dual-mode inhibition of the ABC transporter MsbA. Nature 557: 196-201.

Holguin F (2018). Triple CFTR Modulator Therapy for Cystic Fibrosis. N Engl J Med 379: 1671-1672.

Jih K-Y, and Hwang T-C (2013). Vx-770 potentiates CFTR function by promoting decoupling between the gating cycle and ATP hydrolysis cycle. Proceedings of the National Academy of Sciences of the United States of America 110: 4404-4409.

Keating D, Marigowda G, Burr L, Daines C, Mall MA, McKone EF, et al. (2018). VX-445–Tezacaftor–Ivacaftor in Patients with Cystic Fibrosis and One or Two Phe508del Alleles. New England Journal of Medicine 379: 1612-1620.

Kopeikin Z, Sohma Y, Li M, and Hwang T-C (2010). On the mechanism of CFTR inhibition by a thiazolidinone derivative. J Gen Physiol 136: 659.

Kopeikin Z, Yuksek Z, Yang HY, and Bompadre SG (2014). Combined effects of VX-770 and VX-809 on several functional abnormalities of F508del-CFTR channels. Journal of Cystic Fibrosis 13: 508-514.

Langron E, Prins S, and Vergani P (2018). Potentiation of the cystic fibrosis transmembrane conductance regulator by VX-770 involves stabilization of the pre-hydrolytic, O1 state. Br J Pharmacol 175: 3990-4002.

Langron E, Simone MI, Delalande CMS, Reymond J-L, Selwood DL, and Vergani P (2017). Improved fluorescence assays to measure the defects associated with F508del-CFTR allow identification of new active compounds. Br J Pharmacol 174: 525-539.

Li H, Yang W, Mendes F, Amaral MD, and Sheppard DN (2012). Impact of the cystic fibrosis mutation F508del-CFTR on renal cyst formation and growth. Am J Physiol Renal Physiol 303: F1176-F1186.

Lin S-C, Karoly ED, and Taatjes DJ (2013). The human ΔNp53 isoform triggers metabolic and gene expression changes that activate mTOR and alter mitochondrial function. Aging Cell 12: 863-872.

Liu F, Zhang Z, Csanády L, Gadsby DC, and Chen J (2017). Molecular Structure of the Human CFTR Ion Channel. Cell 169: 85-95.e88.

Liu F, Zhang Z, Levit A, Levring J, Touhara KK, Shoichet BK, et al. (2019). Structural identification of a hotspot on CFTR for potentiation. Science 364: 1184-1188.

Liu J, Bihler H, Farinha CM, Awatade NT, Romão AM, Mercadante D, et al. (2018). Partial rescue of F508del-cystic fibrosis transmembrane conductance regulator channel gating with modest improvement of protein processing, but not stability, by a dual-acting small molecule. Br J Pharmacol 175: 1017-1038.

Lukacs GL, and Verkman AS (2012). CFTR: folding, misfolding and correcting the [delta]F508 conformational defect. Trends Mol Med 18: 81-91.

Ma T, Vetrivel L, Yang H, Pedemonte N, Zegarra-Moran O, Galietta LJV, et al. (2002). High-affinity Activators of Cystic Fibrosis Transmembrane Conductance Regulator (CFTR) Chloride Conductance Identified by High-throughput Screening. J Biol Chem 277: 37235-37241.

Matthes E, Goepp J, Carlile GW, Luo Y, Dejgaard K, Billet A, et al. (2016). Low free drug concentration prevents inhibition of F508del CFTR functional expression by the potentiator VX-770 (ivacaftor). British Journal of Pharmacology 173: 459-470.

Meng X, Wang Y, Wang X, Wrennall JA, Rimington TL, Li H, et al. (2017). Two Small Molecules Restore Stability to a Subpopulation of the Cystic Fibrosis Transmembrane Conductance Regulator with the Predominant Disease-causing Mutation. J Biol Chem 292: 3706-3719.

Okiyoneda T, Veit G, Dekkers JF, Bagdany M, Soya N, Xu H, et al. (2013). Mechanism-based corrector combination restores deltaF508-CFTR folding and function. Nat Chem Biol 9: 444-454.

Pedemonte N, Lukacs GL, Du K, Caci E, Zegarra-Moran O, Galietta LJV, et al. (2005a). Small-molecule correctors of defective [Delta]F508-CFTR cellular processing identified by high-throughput screening. J Clin Invest 115: 2564-2571.

Pedemonte N, Sonawane ND, Taddei A, Hu J, Zegarra-Moran O, Suen YF, et al. (2005b). Phenylglycine and Sulfonamide Correctors of Defective [Delta]F508 and G551D Cystic Fibrosis Transmembrane Conductance Regulator Chloride-Channel Gating. Mol Pharmacol 67: 1797-1807.

Phuan P-W, Son J-H, Tan J-A, Li C, Musante I, Zlock L, et al. (2018). Combination potentiator ('co-potentiator') therapy for CF caused by CFTR mutants, including N1303K, that are poorly responsive to single potentiators. Journal of Cystic Fibrosis.

Phuan P-W, Veit G, Tan J, Finkbeiner WE, Lukacs GL, and Verkman AS (2015). Potentiators of Defective ΔF508-CFTR Channel Gating that do not Interfere with Corrector Action. Mol Pharmacol 88: 791-799.

Phuan P-W, Yang B, Knapp JM, Wood AB, Lukacs GL, Kurth MJ, et al. (2011). Cyanoquinolines with Independent Corrector and Potentiator Activities Restore [delta]Phe508-Cystic Fibrosis Transmembrane Conductance Regulator Chloride Channel Function in Cystic Fibrosis. Mol Pharmacol 80: 683-693.

Ratner M (2017). FDA deems in vitro data on mutations sufficient to expand cystic fibrosis drug label. Nature Biotechnology 35: 606.

Rennolds J, Boyaka PN, Bellis SL, and Cormet-Boyaka E (2008). Low temperature induces the delivery of mature and immature CFTR to the plasma membrane. Biochem Biophys Res Commun 366: 1025-1029.

Riordan JR, Rommens JM, Kerem B, Alon N, Rozmahel R, Grzelczak Z, et al. (1989). Identification of the cystic fibrosis gene: cloning and characterization of complementary DNA. Science 245: 1066-1073.

Rommens JM, Iannuzzi MC, Kerem B-s, Drumm ML, Melmer G, Dean M, et al. (1989). Identification of the Cystic Fibrosis Gene: Chromosome Walking and Jumping. Science 245: 1059-1065.

Rowe SM, and Verkman AS (2013). Cystic Fibrosis Transmembrane Regulator Correctors and Potentiators. Cold Spring Harb Perspect Med 3: a009761.

Saint-Criq V, and Gray MA (2017). Role of CFTR in epithelial physiology. Cellular and Molecular Life Sciences 74: 93-115.

Shaner NC, Campbell RE, Steinbach PA, Giepmans BNG, Palmer AE, and Tsien RY (2004). Improved monomeric red, orange and yellow fluorescent proteins derived from Discosoma sp. red fluorescent protein. Nat Biotechnol 22: 1567.

Sigoillot M, Overtus M, Grodecka M, Scholl D, Garcia-Pino A, Laeremans T, et al. (2019). Domain-interface dynamics of CFTR revealed by stabilizing nanobodies. Nature Communications 10: 2636.

Solomon GM, Fu L, Rowe SM, and Collawn JF (2017). The therapeutic potential of CFTR modulators for COPD and other airway diseases. Current Opinion in Pharmacology 34: 132-139.

Solymosi EA, Kaestle-Gembardt SM, Vadász I, Wang L, Neye N, Chupin CJA, et al. (2013). Chloride transport-driven alveolar fluid secretion is a major contributor to cardiogenic lung edema. Proceedings of the National Academy of Sciences of the United States of America 110: E2308-E2316.

Sosnay PR, Siklosi KR, Van Goor F, Kaniecki K, Yu H, Sharma N, et al. (2013). Defining the disease liability of variants in the cystic fibrosis transmembrane conductance regulator gene. Nat Genet 45: 1160-1167.

Thiagarajah JR, Donowitz M, and Verkman AS (2015). Secretory diarrhoea: mechanisms and emerging therapies. Nat Rev Gastroenterol Hepatol 12: 446-457.

Thibodeau PH, Richardson JM, Wang W, Millen L, Watson J, Mendoza JL, et al. (2010). The Cystic Fibrosis-causing Mutation deltaF508 Affects Multiple Steps in Cystic Fibrosis Transmembrane Conductance Regulator Biogenesis. J Biol Chem 285: 35825-35835.

Van Goor F, Hadida S, Grootenhuis PDJ, Burton B, Cao D, Neuberger T, et al. (2009). Rescue of CF airway epithelial cell function in vitro by a CFTR potentiator, VX-770. Proceedings of the National Academy of Sciences of the United States of America 106: 18825-18830.

Van Goor F, Hadida S, Grootenhuis PDJ, Burton B, Stack JH, Straley KS, et al. (2011). Correction of the F508del-CFTR protein processing defect in vitro by the investigational drug VX-809. Proceedings of the National Academy of Sciences of the United States of America 108: 18843-18848.

Van Goor F, Straley KS, Cao D, Gonzalez J, Hadida S, Hazlewood A, et al. (2006). Rescue of [Delta]F508-CFTR trafficking and gating in human cystic fibrosis airway primary cultures by small molecules. Am J Physiol Lung Cell Mol Physiol 290: L1117-1130.

Van Goor F, Yu H, Burton B, and Hoffman BJ (2014). Effect of ivacaftor on CFTR forms with missense mutations associated with defects in protein processing or function. J Cyst Fibros 13: 29-36.

Veit G, Avramescu RG, Perdomo D, Phuan P-W, Bagdany M, Apaja PM, et al. (2014). Some gating potentiators, including VX-770, diminish F508del-CFTR functional expression. Sci Transl Med 6: 246ra297.

Wainwright CE, Elborn JS, Ramsey BW, Marigowda G, Huang X, Cipolli M, et al. (2015). Lumacaftor–Ivacaftor in Patients with Cystic Fibrosis Homozygous for Phe508del CFTR. N Engl J Med 373: 220-231.

Wang X, Koulov AV, Kellner WA, Riordan JR, and Balch WE (2008). Chemical and Biological Folding Contribute to Temperature-Sensitive ΔF508 CFTR Trafficking. Traffic 9: 1878-1893.

Wang Y, Cai Z, Gosling M, and Sheppard DN (2018). Potentiation of the cystic fibrosis transmembrane conductance regulator Cl− channel by ivacaftor is temperature independent. American Journal of Physiology-Lung Cellular and Molecular Physiology 315: L846-L857.

Yang H, Shelat AA, Guy RK, Gopinath VS, Ma T, Du K, et al. (2003). Nanomolar Affinity Small Molecule Correctors of Defective [Delta]F508-CFTR Chloride Channel Gating. J Biol Chem 278: 35079-35085.

Yu H, Burton B, Huang C-J, Worley J, Cao D, Johnson Jr JP, et al. (2012). Ivacaftor potentiation of multiple CFTR channels with gating mutations. J Cyst Fibros 11: 237-245.

Zhang J, Wang Y, Jiang X, and Chan HC (2018a). Cystic fibrosis transmembrane conductance regulator—emerging regulator of cancer. Cellular and Molecular Life Sciences 75: 1737-1756.

Zhang Z, Liu F, and Chen J (2018b). Molecular structure of the ATP-bound, phosphorylated human CFTR. Proceedings of the National Academy of Sciences of the United States of America.

Zhao R, Liang X, Zhao M, Liu S-L, Huang Y, Idell S, et al. (2014). Correlation of Apical Fluid-Regulating Channel Proteins with Lung Function in Human COPD Lungs. PLOS ONE 9: e109725.

Figures and figure legends

Figure 1

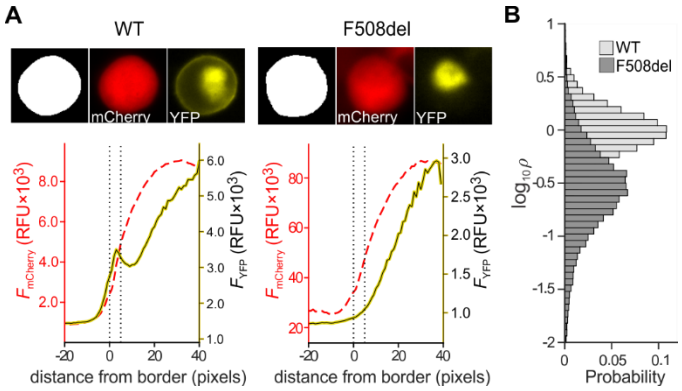

Image analysis to quantify CFTR membrane density (**A**) Image analysis of individual representative HEK293 cells transfected with pIRES2-mCherry-YFP-WT-CFTR (left), and pIRES2-mCherry-YFP-F508del-CFTR (right). Upper panels: boundary delimiting cell (white) from non-cell (black) is obtained from mCherry image (centre). CFTR cellular localization is obtained from YFP image (right). Lower panels: average mCherry fluorescence intensity (F_{mCherry}, red dashed line), and average YFP fluorescence intensity (F_{YFP}, solid yellow line), as a function of the distance from cell border. Membrane density is defined as

$$\rho = \frac{F_{\mathrm{YFP\ membrane}}}{F_{\mathrm{mCherry\ cell}}}$$

where $F_{\mathrm{YFP\ membrane}}$ is the average fluorescence intensity within the 'membrane' zone, set between 0 and 5 pixels from the cell border. (**B**) Probability density distribution of $\log_{10}\rho$ for cells expressing YFP-WT-CFTR (light grey), and YFP-F508del-CFTR (dark grey), incubated at 37 °C. For the representative cells shown in panel A, WT: $\rho = 1.60$; F508del: $\rho = 0.25$.

Figure 2

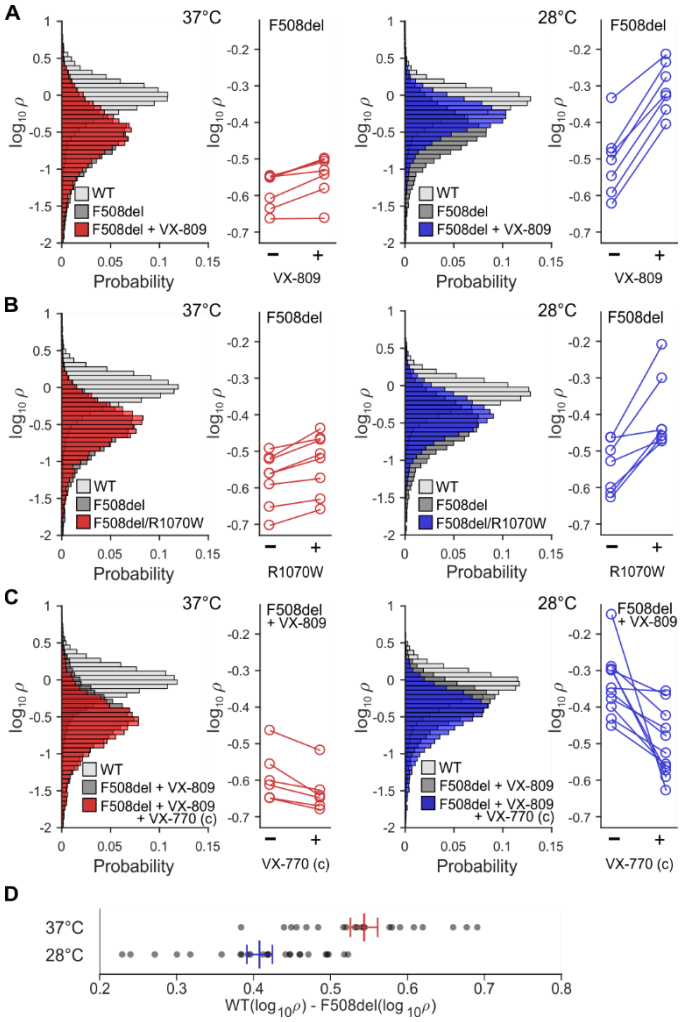

Monitoring CFTR membrane density ($\log_{10}\rho$) in HEK293 cells expressing WT-CFTR, F508del-CFTR, or F508del/R1070W-CFTR. Effects of chronic treatment with 10 µM VX-809 (**A**), R1070W rescue (**B**), and chronic treatment with 10 µM VX-809 + 10 µM VX-770 (**C**), on $\log_{10}\rho$ at 37°C (left, red) and 28°C (right, blue). Conditions of final incubation were maintained during image acquisition. The probability distributions in the panels on the left, contain $\log_{10}\rho$ measurements from thousands of cells, pooled from all experiments. For statistical analysis, mean $\log_{10}\rho$ values determined in independent experiments, and paired per plate, were used (displayed in panels on the right) (**D**) Before imaging, plates were incubated at 37°C, or 28°C for 24 hours. For each plate, the difference between mean $\log_{10}\rho$ for WT-CFTR and F508del-CFTR was calculated (WT($\log_{10}\rho$) - F508del($\log_{10}\rho$), grey dots). Red (37°C) and blue (28°C) lines show mean ± SEM, calculated from 21(37°C) and 25(28°C) within-plate difference estimates.

945 **Figure 3**

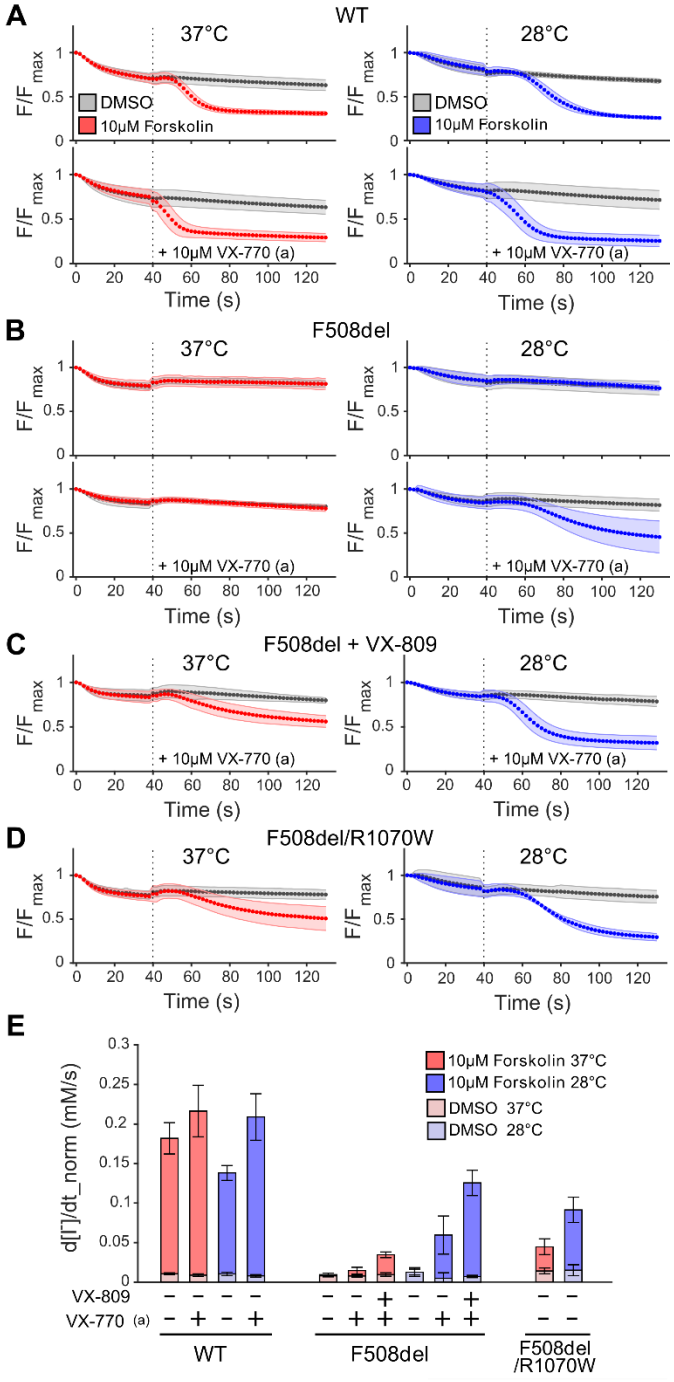

946

947 Monitoring CFTR ion channel function. (**A-D**) Quenching of YFP fluorescence in HEK293
948 cells expressing WT-CFTR (**A**), F508del-CFTR chronically (24 h) treated with DMSO (**B**) or
949 with VX-809 (**C**), and R1070W/F508del-CFTR (**D**). For more information on statistical
950 analysis see Supplementary Tables S2 and S3. Prior to imaging plates were incubated for 24
951 hours, at 37°C (left panels, red) or 28°C (right panels, blue). This final incubation temperature
952 was maintained throughout image acquisition. At time point 0 s I⁻ was added to the extracellular
953 medium. At 40 s forskolin and, where indicated, VX-770 (acute, a) was added (dotted line),

954 both to a final concentration of 10 μM. The fluorescence before addition of I^- (F_{max}), was used
955 to normalize YFP fluorescence intensity. (**E**) The maximal rate of I^- entry (d[I^-]/dt_norm) is
956 used to summarize CFTR function for genotypes and conditions shown in (**A**-**D**).

957 **Figure 4**

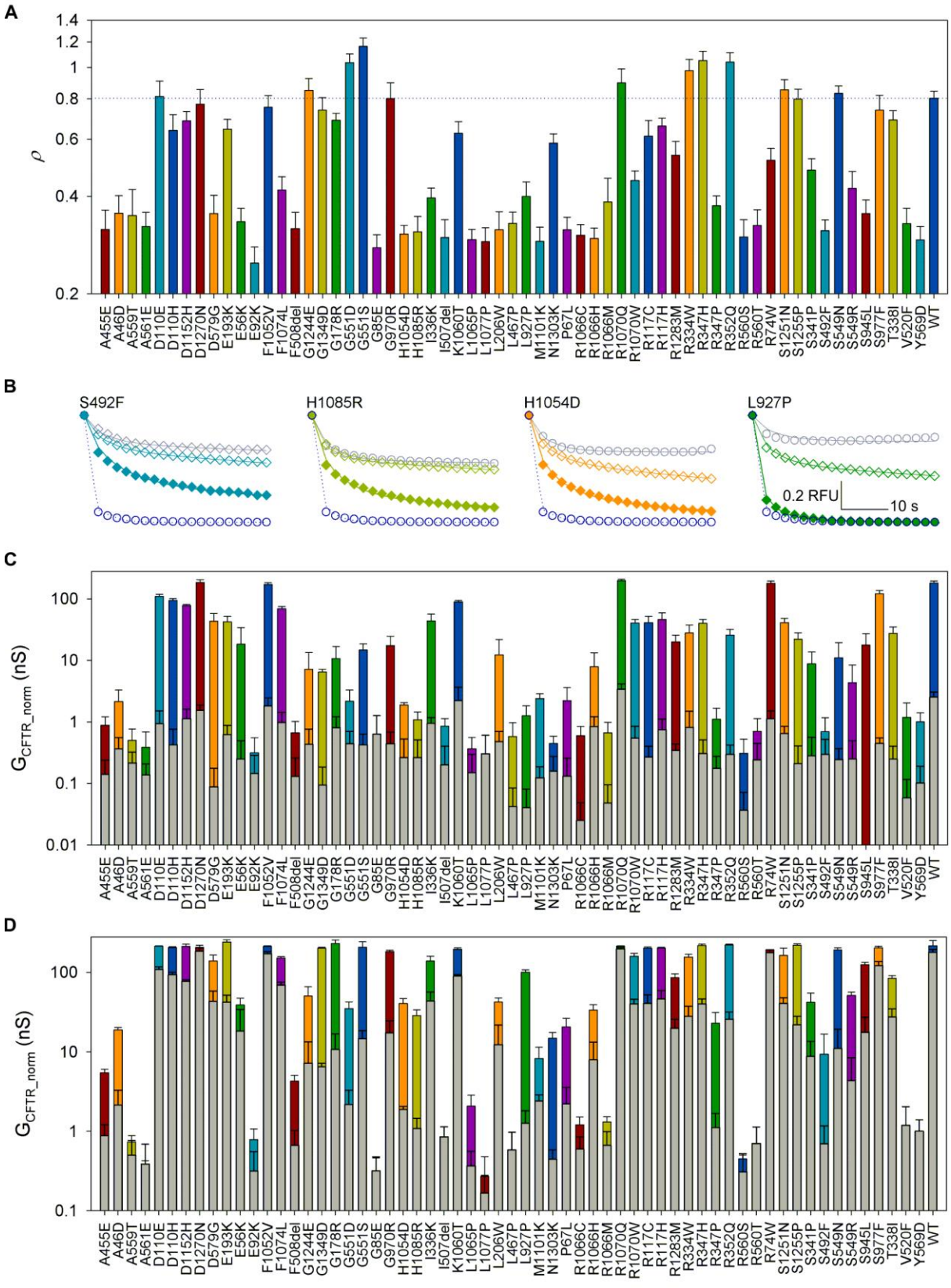

Rare CF-mutation profiling. (**A**) Mean ρ ($n \geq 9$) of all mutations in the panel. Dotted line indicates mean ρ for WT-CFTR. For ρ distributions, mean ρ and n values for each mutant see Supplementary Figure S5 and Supplementary Table S4. (**B**) Observed YFP quenching time course in the presence of DMSO (grey circles) or 10 μM forskolin (empty coloured diamonds), or 10 μM forskolin + acute 10 μM VX-770 (filled coloured diamonds) for selected mutations. Solid lines show predicted change in proportion of anion-free YFP. For estimated parameters G_{CFTR}, V_M, G_{trans} and τ_{trans} see Supplementary Table S10. WT-CFTR quenching in 10 μM forskolin (dark blue empty circles and dotted line) shown for comparison. (**C**) CFTR conductance of rare mutation panel after activation with 10 μM forskolin (coloured bars) or vehicle control (DMSO, grey bars). $n \geq 3$. G_{CFTR} obtained from fitting of quenching time-course for each mutant was normalized using the mean within cell mCherry fluorescence for that mutant, measured with respect to the corresponding metric obtained for WT-CFTR on the same plate. (**D**) Potentiation of rare mutation panel by VX-770. Grey bars show values following activation with 10 μM forskolin alone, coloured bars with further addition of acute 10 μM VX-770. For more information on statistical analysis of quenching data see Supplementary Tables S6 and S7.

974 **Figure 5**

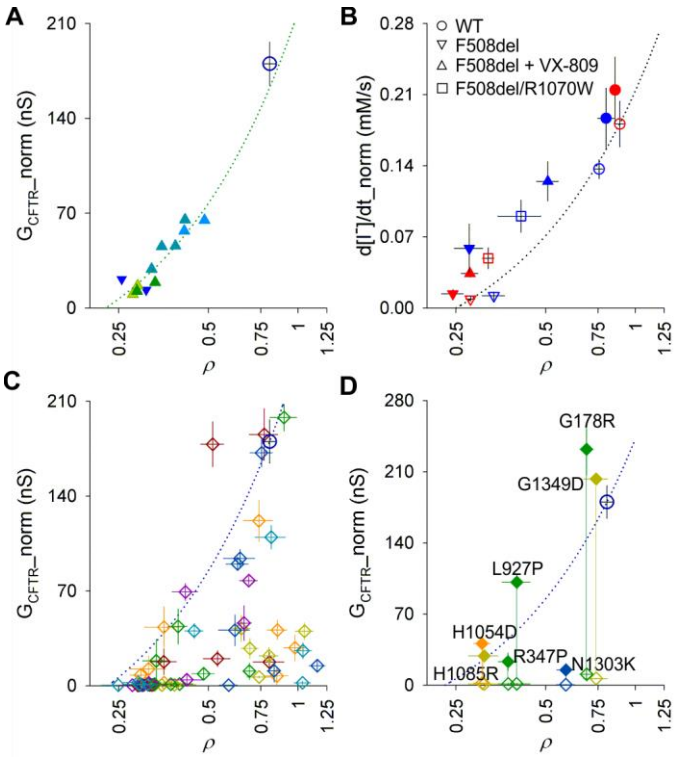

975

976 Investigating permeation/gating characteristics. (**A**) Relationship between normalized CFTR
977 conductance and membrane density in cells expressing F508del-CFTR with no correction (blue
978 ∇) or incubated with increasing concentrations of VX-809 (1 nM to 10 μM, green to light blue
979 Δ), all after activation with 10 μM forskolin and acute potentiation with 10 μM VX-770.
980 F508del-CFTR incubation and measurements were at 28°C. Green dotted line shows linear
981 regression using only F508del-CFTR data points on graph (slope = 281.7, constant = -63.7,
982 resulting in an x-axis intercept at $\rho = 0.23$). Mean value for WT-CFTR activated with 10 μM
983 forskolin alone is shown for reference (from (**C**), large dark blue empty circle). (**B**)
984 Relationship between maximal rate of I^- influx and ρ in HEK293 cells expressing WT-CFTR,
985 F508del-CFTR, and F508del/R1070W-CFTR, at 37°C (red symbols) and 28°C (blue symbols).
986 10 μM forskolin was used to activate CFTR. Empty symbols indicate activation with forskolin
987 alone. Solid symbols indicate further acute potentiation with 10 μM VX-770. Dotted line:
988 linear interpolation between data obtained at 37°C for uncorrected F508del-CFTR (used as an
989 empirical measure of minimal membrane density) and WT-CFTR, both without acute VX-770
990 potentiation; slope = 0.284, constant = -0.071, resulting in an x-axis intercept at $\rho = 0.25$. (**C**)
991 Relationship between baseline G_{CFTR_norm} (10 μM forskolin) and ρ for rare mutation panel.
992 Colours as in Figure 4. WT-CFTR is highlighted as a large, dark blue, empty circle. The dark

993 blue dotted line (slope = 314.1, constant= -72.3) shows linear interpolation between WT data
994 points and x-axis intercept set at ρ =0.23, as obtained in (**A**). (**D**) Mutants with largest fold
995 potentiation by VX-770 (ratio between conductance obtained in 10 μM forskolin + 10 μM VX-
996 770 over that in 10 μM forskolin alone > 20). Empty diamonds indicate baseline activation
997 with 10 μM forskolin alone, solid diamonds indicate activation following acute potentiation
998 with 10 μM forskolin + 10 μM VX-770.

999 **Figure 6**

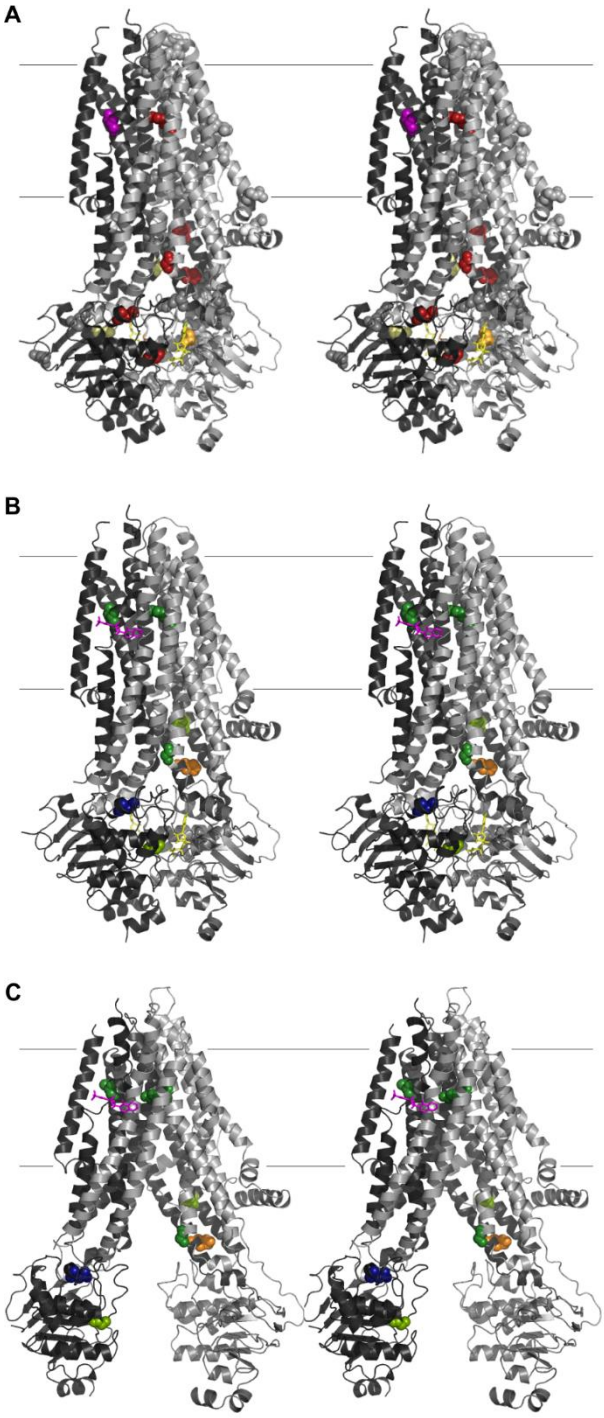

1000

1001 Mapping VX-770 sensitivity on cryo-EM structures. (**A**) Cartoon representation (cross-eye
1002 stereo) of phosphorylated, ATP-bound human CFTR, 6MSM (Zhang et al., 2018b), with sites
1003 of missense mutations in panel highlighted as spheres. Colours indicate degree of VX-770-
1004 potentiaton (fold potentiation, F < 5, grey; 5 < F < 10, white; 10 < F < 15, light yellow; 15 < F
1005 < 20, orange; 20 < F < 50, red; F > 50 purple). TMD1-NBD1 in light grey; TMD2-NBD2 in
1006 dark grey. Fine horizontal lines show approximate position of membrane boundary. (**B**) Only

positions with most efficacious VX-770 potentiation are shown. Magenta sticks show position of bound VX-770 in 6O2P structure (Liu et al., 2019). Mutation-site residues are colour-coded as in Fig. 4 (moving from cytosol to extracellular): G1349, light green; N1303, dark blue; H1054, orange; G178, forest; H1085, light green; R347, forest right; L927 forest left. (**C**) Orientation as in (**A,B**) but using atom coordinates of dephosphorylated human CFTR, 5UAK (Liu et al., 2017).